Multi-Antenna System for In-Line Food Imaging at Microwave Frequencies

Multi-Antenna System for In-Line Food Imaging at Microwave Frequencies

Marco Ricci, *Member, IEEE*, Jorge A. Tobon Vasquez, *Member, IEEE*, Rosa Scapaticci, *Member, IEEE*, Lorenzo Crocco, *Senior Member, IEEE* and Francesca Vipiana, *Senior Member, IEEE*.

***Abstract*—This work presents the design and numerical assessment of a novel microwave imaging system, capable of providing a full 3-D image of food/beverage products content in order to disclose the possible presence of physical contaminants, such as plastic fragments. The system here presented exploits the dielectric contrast between the food content and possible intrusions at microwave frequencies; it is based on an antennas array architecture inspecting the items in motion along a conveyor belt without interrupting the production process. The inversion problem is solved by means of linearization, assuming the viability of the Born approximation thanks to the localized intrusions, and regularization, based on the singular value decomposition of the discretized scattering operator. Further, an algorithm, to balance the illumination of the considered scenario due to the non-uniform radiation of the employed antennas, is presented to enhance the imaging. The system is first assessed considering an ideal case, and then extended to a more realistic approach, for two different kinds of food products, with completely different dielectric properties and considering the performance of existing instrumentation for the purpose. The obtained results lay the foundations for the realization of an actual prototype.**

***Index Terms*—Microwave imaging, microwave antenna arrays, microwave propagation, food technology, inspection, non-invasive diagnostics, food security, food safety.**

I. Introduction

NOWADAYS, there are several technologies employed in industries for packaged food inspection [1], but the presence of physical contaminants in food/beverage products is still a threat, with a growth of notifications mainly due to customers complaints [2].

The most common monitoring devices, exploited along the food packaging line, are metal detectors and X-rays systems. However, metal detectors can only detect metallic objects, while X-rays have limitations in detecting low-density materials [3], [4]. In order to overcome these limitations, "dual-energy" X-rays systems have been developed [5], but they still lack in discerning some kind of materials, and the occurrence of foreign bodies notifications is an indirect confirmation of such a circumstance. In particular, materials based on low-density polyethylene and polypropylene, the most common plastics (with a density below 1 g/cm^3) widely employed in food packaging [6], are still not detectable [7]. Accordingly, there is the need of developing imaging solutions not relying on material densities only, to complement with existing technologies and improve the level of security of food/beverage products.

In this respect, near infra-red (NIR) and THz sensing technologies have been recently applied to food inspection [8]–[12]. These imaging modalities are rapid and safe, due to the use of non-ionizing radiations, but their penetration depth is limited. Hence, these technologies prove to be effective for detecting defects on or close to external surfaces, as e.g. packaging imperfections, but they are not suitable to properly inspect the inner content of food/beverage products to detect potential contaminants.

In the last decade, microwave imaging (MWI) attracted increasing interest in food industry [13]–[16]. Its principle is based on the alteration of the penetrating electromagnetic (EM) non-ionizing waves within a volume of interest due to the presence of a contaminant. This results from the dielectric difference, at microwave frequencies, between the food product under test and the contamination, that, if present, is capable of a slight modification of the penetrating EM waves. The product under analysis is illuminated with low-power EM waves, which are then captured at the receivers locations and properly analyzed, in order to feed ad-hoc algorithms which are capable to translate the signal into a tomographic image of the contaminant. MWI technology is non-destructive, since the employed power level does not alter the food product, and it is capable of penetrating objects up to few centimeters depending on the working frequency, thus making it suitable for most packaged food products. This is valid in the case of non-metallic packaging. Hence, MWI technology can be investigated to fill the deficiency in existing diagnostic means adopted to ensure packaged food safety along the production chain. In particular, this technology has the potential of detecting certain classes of contaminants that are still not visible with existing commercial inspection systems, such as low-density plastic fragments [7]. The final aim is to avoid any kind of health hazards for consumers as well as to avoid expensive food recalls and even to prevent a loss of customers confidence in a brand for food producers.

This paper presents the design and the numerical assessment of a novel and, to the best of our knowledge, unique MWI system for monitoring food products, built up with an array of antennas. The device is thought to fit along a production line

Manuscript received XXX, 2021; accepted XXX. Date of publication XXX; date of current version XXX. This work was supported by the Italian Ministry of University and Research under the PRIN project "BEST-Food, Broadband Electromagnetic Sensing Technologies for Food quality and security assessment". *(Corresponding author: Francesca Vipiana)*

J. A. Tobon Vasquez, M. Ricci and F. Vipiana are with the Department of Electronics and Telecommunications, Politecnico di Torino, 10129 Torino, Italy (e-mail: francesca.vipiana@polito.it).

R. Scapaticci and L. Crocco are with the Institute for the Electromagnetic Sensing of the Environment, National Research Council of Italy, 80124 Napoli, Italy (e-mail: crocco.l@irea.cnr.it).

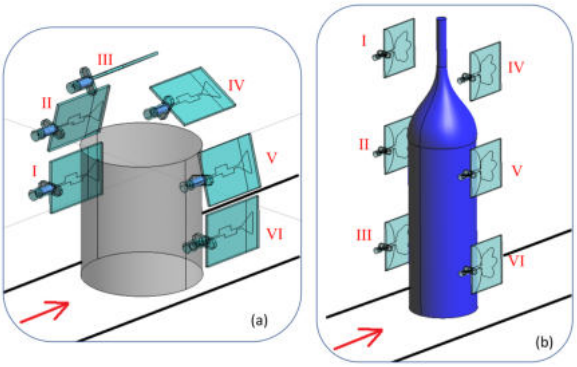

Fig. 1. The considered antenna array configurations; (a): arch configuration, implementing a tunnel-shaped architecture; (b): two opposed lines configuration, implementing a canyon-shaped architecture. In both figures, the product under test is also shown.

without interrupting the process. Preliminary studies related to the development of the system have been conducted in [17], [18], and its principles have been illustrated in [15]. From the latter, this work differs for the use of a multi-view architecture, the use of suitable acquisition strategies and an enhanced imaging tool. A deep analysis, in which features and architecture of the MWI system are described, is presented in this work, as well as a detailed analysis of the system behavior with the food product in motion along the line. In particular, to consider different kinds of food products, two conformal array configurations sharing the same complexity (i.e., number of antennas) have been considered in this study. In the first one, shown in Fig. 1(a), the antennas are displaced along an arch, whereas in the second one, shown in Fig. 1(b), they are positioned along two lines. Taking advantage of the motion of the target along the conveyor belt, the two configurations correspond to a synthetic array having the shape of a "tunnel" and a "canyon", respectively. Hence, the system is capable to collect data along a (virtual) surface and therefore provide a full 3-D image of the product.

On the other hand, the movement of the target also poses a definite constraint in the design of the system. As a matter of fact, the trade-off between the need of acquiring as much information as possible and the need of performing them in the shortest time possible must be addressed. To this end, similarly to [15], taking into account the acquisition rate of the network analyzer and the velocity of the items on the conveyor, it is possible to estimate the length of the allowed acquisition window (which corresponds to the number of positions of the target which can be considered). In addition, in order to exploit the data diversity offered by the array architecture, different acquisition strategies have been implemented and compared, to define the most convenient one from the point of view of the imaging results. The imaging step is implemented through a real-time inversion algorithm, based on the distorted Born approximation. It has been further enhanced through an ad-hoc post-processing; its principle is based on the equalization of reconstruction values, given that the illumination of employed antennas is non-uniform in the region under test. Finally, the imaging performance of the designed systems have been numerically assessed for oil-based packaged food products (hazelnut-cocoa cream) and water bottles.

The paper is organized as follows. Section II presents the architecture of the system, its design and the data acquisition strategies, as well as the proposed imaging approach. In Sect. III, the designed antenna array configurations are analyzed in detail to prove their feasibility, by performing their assessment via numerical simulations carried out in ideal conditions and in a realistic scenario. Finally, in Sect. IV, the conclusions and the foreseen next steps are summarized.

II. Microwave Imaging System Design and Architecture

The proposed system is meant to provide a real-time output in detecting a contaminated item, by fitting existing production lines without delaying their operation. Hence, it has to be capable of analyzing packaged food products moving on a conveyor belt at the speed employed in industrial plants. To this end, the system is made of an antenna array that can be connected to a multi-port vector network analyzer (VNA) [19], in order to acquire the scattering matrices at the different time instants while the target is moving along the conveyor belt. The designed array is formed by low-cost monopole printed antennas tuned to work at the proper frequency, that, via their omnidirectional radiation pattern [20], can illuminate the whole region of interest along the conveyor belt.

The first issue, that has to be addressed in the design of the system, is to determine the suitable number of array elements, i.e., the number of elements such to acquire as much information as possible, while reducing the system's complexity and being, in any case, non-redundant. Such an issue can be addressed using the approach adopted for biomedical imaging systems design [21]–[25] based on the band-limited properties of EM fields [26]. In particular, the approach has been herein applied as follows. First, given the geometrical size of the cross-section of the target intersecting the plane of the array, the number of samples needed to measure the field radiated by a source having the same size as the target on a closed curve that encloses it (e.g. a circumference) is estimated. Such a number is well approximated by the ratio $N_o = 2P/\lambda$, with P being the perimeter of the target cross-section and λ the wavelength in free space at the frequency of operation. As stated in [27], [28], considering the degrees of freedom theory, N_o represents the number of needed samples to non-redundantly evaluate the field radiated from a source enclosed in a perimeter P curve. Applying this to imaging, the output number gives an approximation of the needed number of antennas to retrieve independent and non-redundant data. Then, as the constraints imposed by the presence of the conveyor belt entail that only a portion of the closed curve can be actually covered by the array, the obtained number is reduced accordingly[1].

[1]It is worth noting that, in the design of an MWI system some tolerance can be accepted in the exact estimation of the degrees of freedom of the field, since the goal is not to collect the samples to *exactly* reconstruct the field, but rather determine a suitable number of independent measurements such to catch as much information as possible on the target also given practical constraints, i.e. the physical size of the antennas and other geometrical constraints such as the impossibility of accessing the target from all sides.

TABLE I
CONSIDERED MEDIA DIELECTRIC FEATURES.

	ε_r	σ	Operating frequency	Penetration depth
Hazelnut-cocoa cream	2.86	0.21 S/m	10.00 GHz	4.28 cm
Water	77.00	1.06 S/m	2.25 GHz	4.41 cm

As mentioned in Sect. I, two array configurations, the arch and two opposed lines architectures (see Fig. 1), and two kind of targets have been considered in this study. In addition, the two targets are referred to different food products. The combination of these elements is considered to determine the number of array elements to be considered.

The target imaged by the arch array is a jar (see Fig. 1(a)), which is assumed to host oil-based food products. This kind of materials is characterized by a low relative permittivity ($\epsilon_r \approx 3$ in the frequency range $1 - 20$ GHz) [15]. Accordingly, the working frequency is set as 10 GHz, as a trade-off between the need of allowing an effective penetration of the probing wave in the target and the need of achieving a high spatial resolution for the microwave imaging algorithm [29]. The dielectric features are resumed in Table I, first row. The cross-section of the cylindrical jar is a rectangle with sides 6.6 cm and 7.5 cm, respectively. Using such numbers, one gets $N_o \approx 18$. Considering the presence of the conveyor belt and the physical size of the antennas, the arch array covers the upper portion of the jar. Accordingly the upper bound for the number of antennas is 9. Finally, considering that VNAs have an even number of port, the need of keeping space between the antennas to reduce mutual coupling and the fact the actual target of the imaging is a very tiny fraction of the jar size, an array of 6 elements is chosen for this configuration.

The second designed antenna array configuration is formed by two opposed lines of elements (see Fig. 1(b)), to image water bottles, which is representative of several food/beverage products composed by water. As water presents high losses at microwave frequencies, a lower working frequency is selected with respect to the previous case. In particular, the designed antenna minimum reflection coefficient is at 2.25 GHz, which is therefore chosen as system working frequency to improve the EM penetration in the water content (as shown in Table I, second row).A common sized bottle is considered, whose cross-section is enclosed in a rectangle having sides of 6.75 cm and 30 cm, respectively. Using such numbers, one gets $N_o \approx 11$, which corresponds to an upper bound for the actual number of antennas of about 5. According to the same considerations as above, an array of 6 evenly spaced elements (three on each side of the belt) is chosen also for this configuration.

It is worth noting that, since the two considered architectures share the same of kind of antennas, i.e. low-cost monopole printed antennas, in the following we will concentrate on the arch array for an in depth analysis, while a single validation example is shown for the other case.

A. Acquisition Strategy

The second issue, that has to be considered in the design of the MWI system, is the motion of the target. By taking advantage of a synthetic aperture approach, the motion provides an increase of the available data, but it also poses constraints on the device, in terms of measurement time and acquisition strategies.

In principle, assuming that, during the time the target approaches and passes the array 6 positions are measured, a total of 36×6 scattering parameters could be acquired. However, as the typical speed of industrial packaging lines is around 50 cm/s for the case of jars [15] and around 100 cm/s for the case of bottles, such a number of measurements can hardly be performed assuming that the target is still in each position.

With a 6-ports VNA, where each antenna is connected to one port, the signal transmitted by one antenna is received in parallel by all the others. The cycle time for the measurement completion (including data transfer) is equal to 1.2 ms, as stated in the specifications at [19] for the frequency range between 1 and 10 GHz (201 points) and using an intermediate frequency (IF) filter of 1 MHz.[2] Such a measurement time is well-suited to assume that the target is still when one antenna in the array is transmitting and the antenna itself and the other five are receiving the back scattered signals; however, the overall time becomes unfeasible to measure the full (6×6) scattering matrix. Accordingly, the acquisition strategy implemented for the proposed device consists in measuring 6 scattering parameters for each position of the target out of the 36 which would be actually available.

Considering that the array is formed by 6 antennas and 6 jar positions are taken, a huge amount of transmitting (TX) antenna versus jar position sequences can be foreseen. Among the various possibilities, three options, called in the following "linear", "alternate" and "external", have been considered in this study. In the linear sequence, the TX antennas are selected along the arch-shaped array according to the progress of the jar along the conveyor belt. In the alternate sequence, the TX antennas follow a different series alternating from the two sides of the arch. Finally, in the external sequence, only the most external (opposite) antennas are used as transmitters. The adopted sequences are summarized in Table II, whereas the numbering of the considered TX antennas is shown in Fig. 1(a). Moreover, in Fig. 2, the linear sequence is graphically represented, depicting in green the selected TX antennas; this is equivalent as considering the object stationary with a spiral-shaped tunnel above it.

TABLE II
CONSIDERED TX ANTENNA / JAR POSITION SEQUENCE.

Linear		**Alternate**		**External**	
Jar position	TX antenna	Jar position	TX antenna	Jar position	TX antenna
1	I	1	VI	1	VI
2	II	2	IV	2	I
3	III	3	II	3	VI
4	IV	4	V	4	I
5	V	5	III	5	VI
6	VI	6	I	6	I

[2]Actually, to reduce the noise level, a narrower IF filter, with much less frequency points, ideally just one point, is expected to be used in practice.

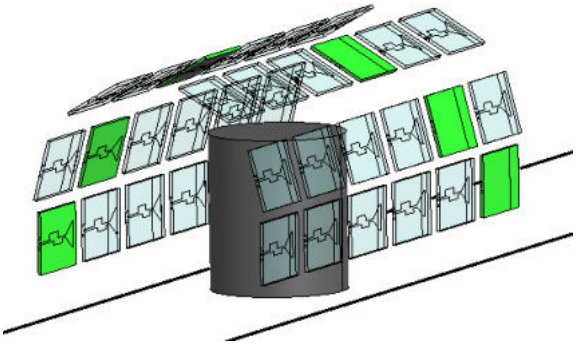

Fig. 2. Equivalent scenario, considering the jar in a fixed position and replicating the antenna array along the line; the linear sequence is graphically represented, depicting in green the selected TX antennas. All distances are here enlarged for visualization purposes, the exact distances for the case under test are reported in Fig. 3(a).

As for the positions in which the targets are measured, in the case of the jar, taking into account the conveyor belt velocity of 50 cm/s and assuming a time for each data acquisition set of scattering parameters of around 13 ms (that is a safety margin with respect to the VNA optimal performance [19]), the jar moves of $\Delta = 2/3$ cm along the line with respect to the previous position, as shown in Fig. 3(a). With this setup, the minimum data acquisition window is around 10 cm, that corresponds to the jar diameter plus five times Δ. This space window corresponds to the minimum required spacing between jars to avoid data acquisition inferences. However, it could be also reduced, including in the imaging procedure more than one jar, but this is outside the scope of the present paper. For the case of a bottle, since the belt moves twice faster, i.e. 100 cm/s, the spacing between two consecutive positions is $\Delta = 4/3$ cm and the data acquisition window is around 14 cm, as shown Fig. 3(b).

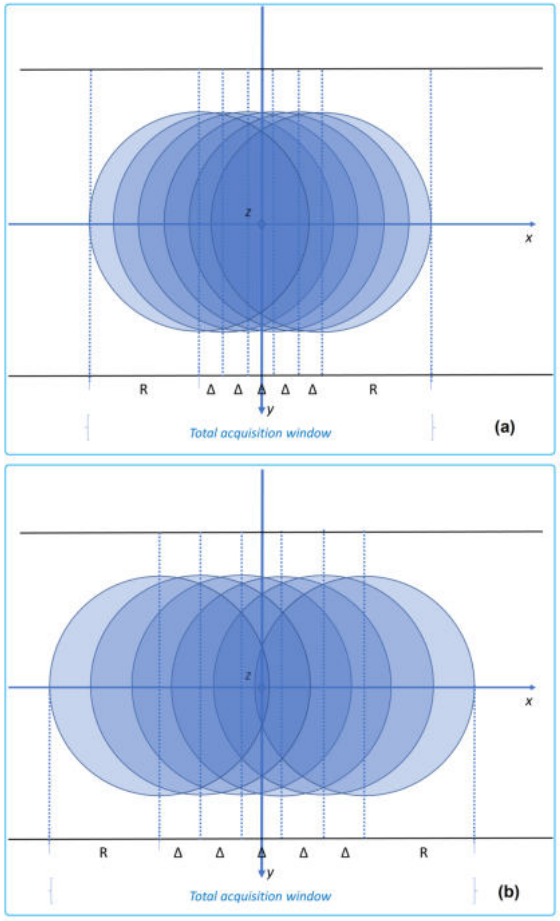

Fig. 3. Target under test positions along the belt during the data acquisition; the target movement is along the x axis, the antenna array is placed at $x = 0$, and the total data acquisition time is around 13 ms. (a): jar positions with motion speed equal to 50 cm/s, $\Delta = 2/3$ cm and $R = 3.3$ cm. (b): bottle positions with motion speed equal to 100 cm/s, $\Delta = 4/3$ cm and $R = 3.375$ cm.

B. Imaging Procedure

The idea behind the proposed imaging procedure is that all the items are equal; thus, it is possible to fix a *reference* scenario given by the uncontaminated product and process the signal obtained by subtracting the reference scattering parameters from the one measured for each item under test. The resulting differential scattering parameters can be intended as the effect of the contamination only, so that by its processing it is possible to image the contamination, as long as the useful signal is not overcome by noise.

Since the goal is to detect small inclusions, e.g. plastic fragments, the overall scattering phenomenon can be well-described by means of the distorted-Born approximation [29], and the underlying imaging problem casts as the inversion of the linear and compact operator $\mathcal{L}$ as

$$\begin{aligned} \Delta S(\mathbf{r}_p, \mathbf{r}_q) &= \mathcal{L}\{\Delta\chi\} \\ &= \frac{-j\omega\epsilon_b}{2\, a_p a_q} \int_D \mathbf{E}_b(\mathbf{r}_p, \mathbf{r}) \cdot \mathbf{E}_b(\mathbf{r}, \mathbf{r}_q)\, \Delta\chi(\mathbf{r})\, d\mathbf{r} \end{aligned} \tag{1}$$

where ΔS represents the differential scattering data, $\mathbf{r}_p$ and $\mathbf{r}_q$ are the positions of transmitting and receiving antennas respectively, j is the imaginary unit, ω is the angular frequency, ϵ_b is the complex permittivity of the background medium (i.e. the uncontaminated food product), and a_p and a_q are the known incoming root-power waves at the p and q antenna ports respectively [30], [31]. Inside the integral, $\mathbf{r}$ is the position within the domain of interest D, "$\cdot$" implies the dot product between vectors and $\mathbf{E}_b$ is the electric field vector in $\mathbf{r}$ radiated by the antenna in $\mathbf{r}_p$ or $\mathbf{r}_q$ within the reference scenario. Finally, $\Delta\chi$ represents the dielectric contrast between the food product and the contamination, defined as the difference between the complex permittivities, in each point $\mathbf{r}$ of D, in the case of the reference scenario and in the case under test, divided by ϵ_b.

The solution of (1) is evaluated via its discretized counterpart:

$$[\Delta S] = [L][\Delta\chi], \tag{2}$$

where $[\Delta S]$ is an N-size column vector that collects the differential scattering parameters evaluated for the considered N antenna pairs, $[\Delta\chi]$ is an M-size column vector containing the dielectric contrast evaluated in the M points that discretize the domain D. $[L]$ is an $N \times M$ matrix whose entries are

given by the discretized version of the scattering operator $\mathcal{L}$, computed by means of the finite element method (FEM) technique [32], [33], with $N = 6 \times P$, P being the number of acquisitions done for each position of the target. In the *ideal* case, in which the full (6×6) scattering matrix for each target position can be measured, assuming that all the transmitters can be used for each of the considered positions, P is equal to 36, whereas P is equal to 6 with the acquisition strategy described in Sect. II-A, in a more realistic consideration in which for each position a single transmitter is active.

Equation (2) is ill-conditioned and it has to be solved in a regularized sense. To this end, the truncated singular value decomposition (TSVD) scheme [34] is exploited and the estimated dielectric contrast, computed as

$$[\Delta\chi] = \sum_{n=1}^{T} \frac{1}{\sigma_n} \langle [\Delta S], [u_n] \rangle [v_n] \tag{3}$$

wherein σ_n, $[u_n]$ and $[v_n]$ are the *n-th* singular value and right and left singular vectors of $[L]$, respectively, and T is the truncation index, chosen in order to adequately trade-off between reconstruction stability (concerning data noise and modeling inaccuracies) and image definition (in terms of resolution) [34].

C. Illumination Balancing Algorithm

We can observe that the volume under test is not evenly illuminated by the antenna array because, during the movement, it has different relative positions with respect to the antennas and the antennas themselves radiate a field not fully uniform in space. Consequently, the illumination of the volume under test is not balanced, with portions more highlighted than others. Hence, in order to enhance the image reconstruction, an algorithm, called in the following illumination balancing algorithm (IBA), has been developed and applied to the discretized operator to smooth the antenna illumination.

The IBA exploits information which can be extracted from the scattering operator singular value decomposition. First, we define the spatial coverage of the scattering operator [35] as

$$[C]_m = \frac{\sum_{n=1}^{T} |[v_n]_m|^2}{\max_m \left[\sum_{n=1}^{T} |[v_n]_m|^2 \right]}, \quad \text{with } m = 1, \ldots, M, \tag{4}$$

where $[C]_m$ and $[v_n]_m$ are the m-th element of the spatial coverage $[C]$ and of the n-th right singular vector $[v_n]$ of the scattering operator, respectively. The spatial coverage $[C]$ can be interpreted as a measure of how well a point in the volume under test is illumined by the antenna array, that is reflected in the quality of the corresponding reconstructed dielectric contrast $[\Delta\chi]$. The values $[C]_m$ depend on the employed antennas and their relative positions with respect to the volume under test.

According to (4), the reconstructed $[\Delta\chi]$ can be improved via a more balanced coverage in the considered volume. The interval $(0, 1)$, spanned by the spatial coverage (4), is subdivided into N sub-intervals defined as $\left[\left(0, \frac{1}{N}\right), \ldots, \left(\frac{n}{N}, \frac{n+1}{N}\right), \ldots, \left(\frac{N-1}{N}, 1\right)\right]$. This subdivision can be interpreted as a description of how well each element in the volume is illuminated, from least to most covered ones respectively. Then, a weight $w_n = \frac{1}{n}$, with $n = 1, \ldots, N$, is assigned to the corresponding n-th interval. Hence, each element $[C]_m$ of the spatial coverage has a corresponding weight w_n assigned as described. These values depend on the quantization of the inverse normalized coverage values. An array, called $[W]$, with dimensionality M, which is the same of coverage and reconstruction arrays, can be set. It is used to map the corresponding weights for each tetrahedra as specified. Finally, these weights are used to improve the reconstructed dielectric contrast as

$$[\Delta\widetilde{\chi}]_m = [\Delta\chi]_m [W]_m, \quad \text{with } m = 1, \ldots, M, \tag{5}$$

where $[\Delta\widetilde{\chi}]_m$ and $[\Delta\chi]_m$ are the m-th element of the improved and initial reconstructed dielectric contrast respectively, and $[W]_m$ is the corresponding m-th weight employed to improve the balancing in illumination.

The principle of IBA is to decrease the illumination of the most highlighted portions of the volume under test, in order to make the global coverage more balanced. Of course this approach is independent from the position and matter of the possible contaminant, since it only depends on the antennas layout with respect to the volume under test. Its effectiveness is assessed in Sect. III, where numerical reconstructions will show the improvements obtained by the IBA application.

III. Numerical Assessment

To assess the designed MWI system, first we consider the antenna array in arch configuration (see Fig. 1(a)) and, as food product under test, a cylindrical jar, with height equal to 7.5 cm and diameter 6.6 cm, filled with hazelnut–cocoa cream, that is an example of oil-based food product. The chosen working frequency is 10 GHz, as detailed in Sect. II.

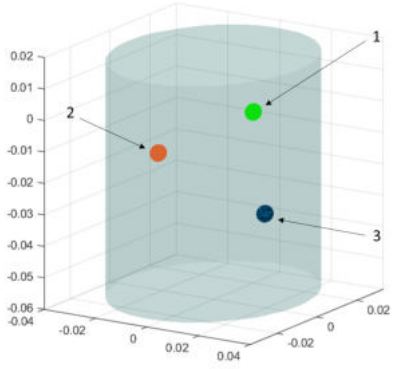

Fig. 4. The three analyzed intrusions positions within the cylindrical jar; each contaminant is reconstructed separately; all dimensions are in meters.

The selected contaminant positions are shown all together in Fig. 4, and reconstructed separately; as contaminant, we select a sphere of polyethylene terephthalate (PET) plastic with 2 mm radius. We choose this dimension because it corresponds to the minimum size contaminants used to test detection systems in food industries [36]. Moreover, the chosen kind of plastic has limited detection with commercial X-ray systems, and,

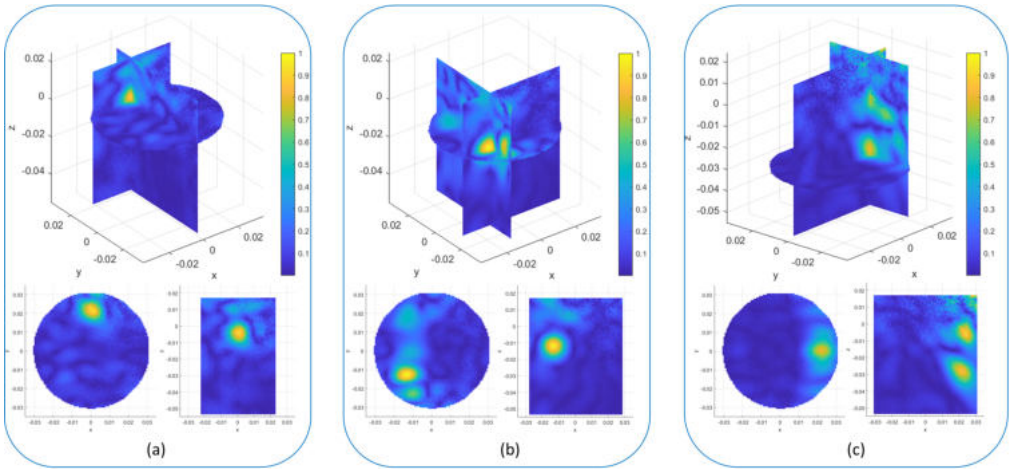

Fig. 5. Normalized dielectric contrast obtained via (6) applied to the three intrusions positions of Fig. 4; (a): intrusion 1, (b): intrusion 2, (c): intrusion 3. All dimensions are in meters.

further, it gives a worst-case scenario in terms of dielectric contrast with respect to the considered hazelnut–cocoa cream. At 10 GHz, the relative permittivity and conductivity of the hazelnut–cocoa cream are equal to 2.86 and 0.21 S/m respectively (see Table I), while the PET plastic relative permittivity is equal to 3.20, with negligible conductivity; hence, the corresponding dielectric contrast amplitude $|\Delta\chi|$, to be detected by the designed MWI system, is equal to 0.17.

A. *Feasibility Study*

First, we consider the *ideal* case where the discretized scattering operator is a $36 \times M$ matrix because, at each jar position, the whole 6×6 scattering parameters are evaluated. This ideal condition would correspond to having a sufficient amount of time to measure a full 6×6 scattering matrix for each of the six jar positions along the conveyor belt. That is clearly unfeasible in a real environment, but it could give important indications of the best MWI system performance as well as its intrinsic limitations.

Moreover, in order to understand the limits of the proposed approach and in particular of the antenna architecture, a preliminary study is performed via the projection of the expected dielectric contrast $[\check{\chi}]$ on the right singular vectors $[v_n]$ of the scattering operator as

$$[\chi] = \sum_{n=1}^{T} \langle [\check{\chi}], [v_n] \rangle [v_n], \tag{6}$$

where the obtained $[\chi]$ is the *best* reconstructed dielectric contrast within the space spanned by the first T singular vectors $[v_n]$. This is obtained by projecting the contrast onto the right singular vectors obtained by the TSVD of the discretized scattering operator, without computing any further scattered data, as it would be in an ideal case.

The three contaminant positions in Fig. 4 are analyzed via (6) and the corresponding normalized dielectric contrast is shown in Fig. 5, where the reconstructed values are pointed in slices over the three planes centered in the exact intrusion position. In Fig. 5(a), contaminant "1" is well reconstructed at its exact position, while, for contaminant "2", Fig. 5(b) shows a slight trace parallel to y-axis and a weaker replica near to the volume boundary. Finally, in Fig. 5(c), the reconstruction of contaminant "3" has a higher replica above the expected intrusion position. Hence, we further analyze the considered scenario evaluating the spatial coverage of the scattering operator via (4), showing in Figs. 6(a) and (b) only the values below 0.01 and 0.005 respectively, where the antenna coverage is lower. In particular, in Fig. 6(b), an arrow highlights the position of intrusion "3", which lays in a part of the volume with a low coverage.

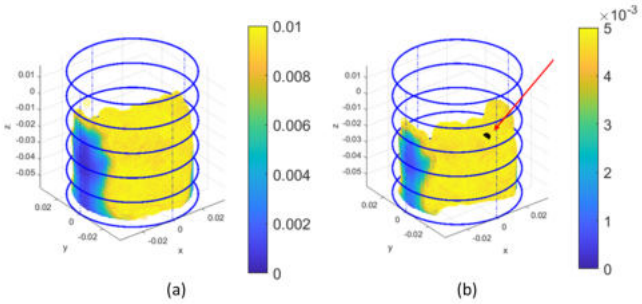

Fig. 6. Spatial coverage for the volume under test with the employed antennas array architecture, obtained through (4); (a): values below 0.01, (b): values below 0.005; all dimensions are in meters.

In order to overcome the shown lack of coverage in some parts of the volume under test (see Fig. 6), the illumination balancing algorithm, described is Sect. II-C, is applied. The IBA allows to improve the quality of dielectric contrast reconstruction, even for contaminant challenging positions, via a re-calibration of the volume coverage in order to flatten it out. The IBA effect on the reconstructed dielectric contrast is shown in Fig. 7 for the three considered contaminants. The first row of Fig. 7 reports the normalized dielectric contrast reconstructed via the TSVD algorithm (3), while, in the second row, the obtained dielectric contrast is re-calibrated via the IBA (5). The three columns of Fig. 7 correspond to the three considered contaminants, respectively. For a better visual

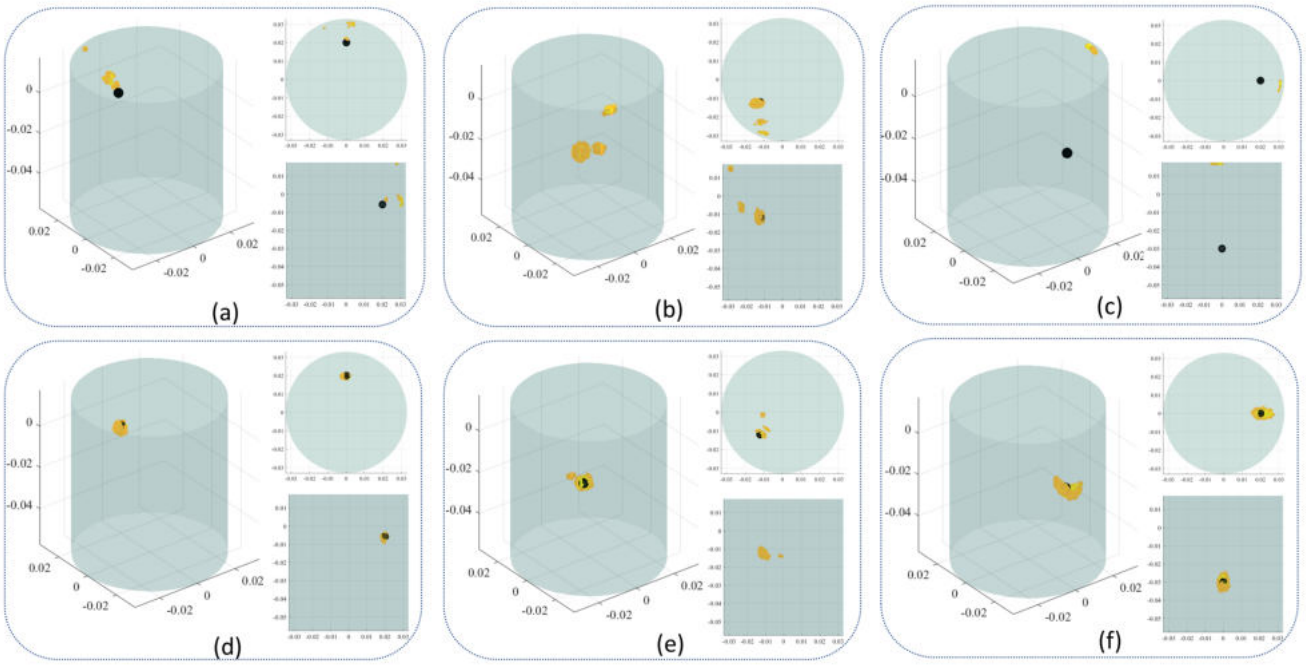

Fig. 7. Normalized dielectric contrast reconstructed via (3); (a)-(c): without IBA, (d)-(f): with IBA; each column corresponds to a different contaminant. In all images the black sphere is the contaminant original position and size, while the yellow circles represent the reconstructed values above 0.8. For each box, isometric, top and side views are shown; all dimensions are in meters.

understanding, all the images in each box show the obtained reconstruction values above a given threshold equal to 0.8 (around -2 dB), after a normalization bringing all values in the interval $(0, 1)$; they are visualized both in xy and yz planes, in addition to an isometric view. The contaminant original position is sketched as a black sphere.

The improvements obtained by the IBA application are quite evident for all the considered contaminant positions. With the IBA, the reconstructed dielectric contrast is less noisy in the case of intrusions "1" and "2", and completely recovered for intrusion "3", where the standard reconstruction approach is not giving the correct position due to lack of spatial coverage. Hence, we verified that the application of the IBA allows to properly identify the contaminant position even in poor coverage zones.

In addition to the visual representation of the reconstructed dielectric contrast, a proximity-based metric is added to better appreciate the detection capabilities of the proposed imaging procedure. The exact position of the contaminant is here known, hence it is possible to evaluate the proximity of the filtered reconstructed values (i.e. normalized values above 0.8) to it, as described in the following equation:

$$P_{V_i} = \frac{N_{r \in V_i}}{N_{tot}} \tag{7}$$

where P_{V_i} is the proximity value for the volume V_i, evaluated as the ratio between $N_{r \in V_i}$, that is the number of filtered reconstruction values inside the considered volume V_i, over the total number of filtered reconstruction values N_{tot}.

Table III reports the evaluated proximity-based metric for the three considered contaminants. The volume V_i is a sphere with radius slightly larger than the contaminant one and in particular it is dictated by the expected resolution in the considered system. As stated in [29], the spatial resolution is limited to half of the wavelength in the medium. Regarding the studied test cases, hazelnut-cocoa cream, the exact value at the chosen frequency is $R_c = \frac{\lambda_{c|10GHz}}{2} = 8.9$ mm. These results are a further confirmation of the enhancement obtained by the application of the illumination balancing algorithm and of the feasibility of the proposed approach for detecting this class of contaminants.

TABLE III
PROXIMITY-BASED METRICS, FEASIBILITY STUDY CASE.

Contaminant Number	Standard Reconstruction	Enhanced Reconstruction
1	21,74%	100%
2	85,57%	95,42%
3	0%	100%

TABLE IV
PROXIMITY-BASED METRICS, REALISTIC SCENARIO.

Cont. Number	Linear Combination	Alternate Combination	External Combination
1	46,74%	59,09%	100%
2	72,29%	55,42%	70,26%
3	100%	100%	100%

B. Realistic Scenario

Once performed the feasibility study of the proposed MWI system in ideal conditions (see Sect. III-A), here we consider a realistic scenario where, at each considered jar position along the conveyor belt, only one antenna is transmitting while all

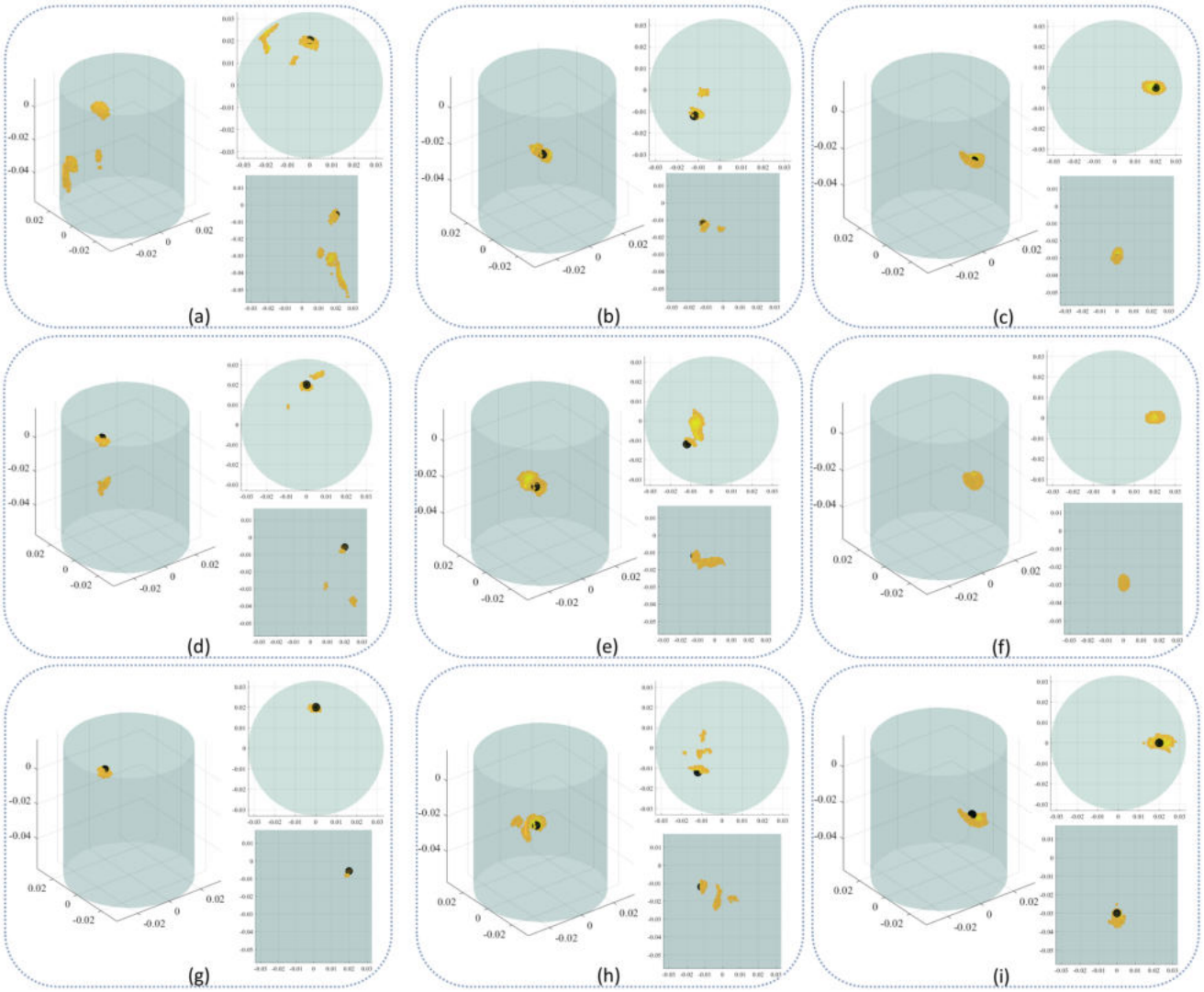

Fig. 8. Normalized dielectric contrast reconstructed via (3) in a realistic scenario for different TX antennas sequence and using IBA; (a)-(c): linear, (d)-(f): alternate, (g)-(i): external; each column corresponds to a different contaminant. In all images the black sphere is the contaminant original position and size, while the yellow circles represent the reconstructed values above 0.8. For each box, isometric, top and side views are shown; all dimensions are in meters.

the others are receiving the signal in parallel; hence, only 6 scattering parameters are computed instead of 36, as detailed in Sect. II-A.

The choice of the tested sequences is representative of a large number of combinations which could have been foreseen. We performed a study of the chosen sequences' spatial coverage capabilities showing that, as expected, there is a slight worsening in performance with respect to the ideal case, but quite similar among each other and to the ideal one too, in terms of portion of the poorly covered volume. The reconstruction results, shown in Fig. 8 and detailed in the next paragraph, confirm the preliminary analysis on the representative chosen sequences, with a marginal enhancement in performance by using the external one, unrelated to the intrusion position.

The normalized dielectric contrast, reconstructed via the TSVD algorithm and enhanced by the IBA in the considered realistic scenario, are shown in Fig. 8. For the three considered contaminant positions (each column of Fig. 8 corresponds to a different contaminant), Figs. 8(a)-(c) shows the reconstructed dielectric contrast employing the linear sequence: even if there is a small amount of noise, in particular noticeable in Fig. 8(a), the object is always detected correctly. The reconstruction is even clearer using the alternate sequence, shown in Figs. 8(d)-(f): in this case the noise is reduced but still present, visible in particular in Fig. 8(e). Finally, with the external sequence shown in Figs. 8(g)-(i), a robust reconstruction is obtained in all the three cases. Then, the corresponding proximity-based metric is reported in Table IV, which confirms that the external sequence is the best option among the three compared ones, apart from contaminant 2: the linear sequence is slightly outperforming but almost equivalent if compared to the external one.

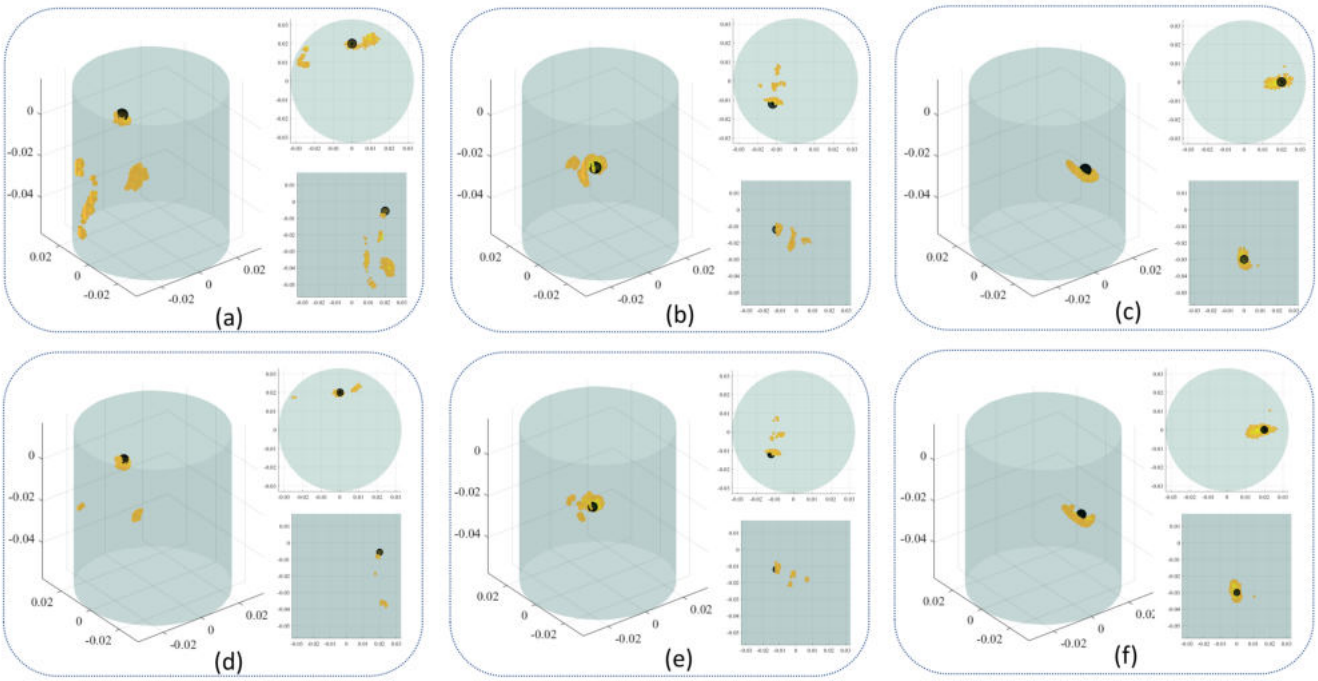

Fig. 9. Normalized dielectric contrast reconstructed via (3) in a realistic scenario and using the external sequence; SNR= 80 dB for (a): intrusion 1, (b): intrusion 2, (c): intrusion 3; SNR= 90 dB for (d): intrusion 1, (e): intrusion 2, (f): intrusion 3. In all images the black sphere is the contaminant original position and size, while the yellow circles represent the reconstructed values above 0.8. For each box, isometric, top and side views are shown; all dimensions are in meters.

C. Effect of noise

In order to make the scenario even more realistic, additive white Gaussian noise (AWGN) is added to the simulated scattering matrices. We consider an input power at the antenna port of 6 dBm, that is within the 6-ports VNA specifications (the maximum output port power is 20 dBm) and a signal-to-noise ratio (SNR) of 80 dB and 90 dB, that corresponds to a noise power of -74 dBm and -84 dBm, both much higher than the VNA noise floor equal to -127 dBm (IF filter equal to 10 Hz) [19].

The normalized reconstructed dielectric contrast, obtained using the external sequence for the selected TX antennas and the corresponding jar positions, is shown in Fig. 9. The AWGN, with SNR= 80 dB, affects mainly the case shown in Fig. 9(a) where some replica are visible inside the volume, but, in all cases, the intrusions are still identified in the expected positions. The reconstruction effectiveness is confirmed in Table V, where a slight worsening of performance with respect to the non-noisy case (see Table IV) appears.

TABLE V
PROXIMITY-BASED METRICS, NOISY SCENARIO, EXTERNAL SEQUENCE.

Contaminant Number	SNR = 80 dB	SNR = 90 dB
1	37,42%	66,67%
2	51,68%	79,1%
3	93,54%	98,38%

D. Lossy medium test case

Lastly, we verified the performance of the proposed MWI approach in the case of water bottles; several food/beverage products are mainly composed by water that has much higher losses, at microwave frequencies, with respect to the previous considered hazelnut–cocoa cream. As described in Sect. II, to analyze water bottles, the working frequency is lowered to 2.25 GHz; at such value, the relative permittivity and conductivity of water are equal to 77 and 1.06 S/m respectively (see Table I). The antenna array architecture is formed by two opposed lines, as shown in Fig. 1(b). A common sized bottle is considered, with a base diameter of 6.75 cm, then shrinking to the neck, with the diameter becoming around 1 cm and an height of 30 cm. The selected sequence is shown in Table VI, according to the TX antennas numbering in Fig. 1(b).

TABLE VI
CONSIDERED TX ANTENNA / BOTTLE POSITION SEQUENCE.

Portal sequence						
Bottle position	1	2	3	4	5	6
TX antenna	VI	IV	II	V	I	III

Moreover, the speed of packaging industrial lines for bottles is double with respect to lines for jars filled with hazelnut–cocoa cream; this speed has been considered for the inter-distance among the different sampling positions accordingly, as specified in Sect. II-A.

As in the case of hazelnut–cocoa cream jars, the contaminant is a 2 mm PET plastic sphere, placed in three positions

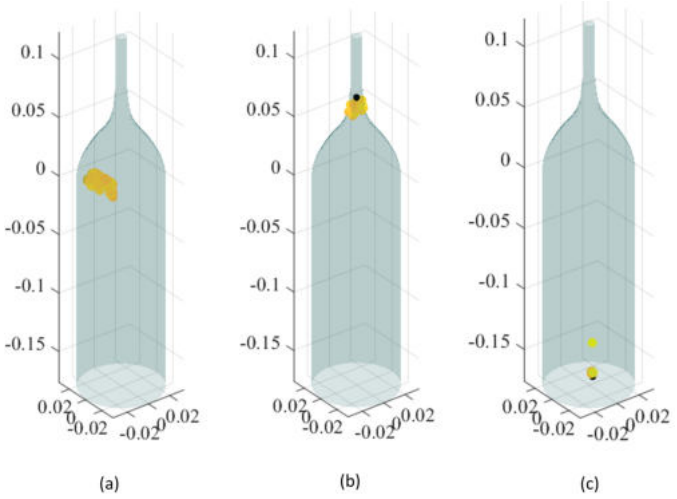

Fig. 10. Normalized dielectric contrast reconstructed via (3) with SNR= 80 dB; (a): intrusion 1, (b): intrusion 2, (c): intrusion 3. In all images the black sphere is the contaminant original position and size, while the yellow circles represent the reconstructed values above 0.8. All dimensions are in meters.

TABLE VII
PROXIMITY-BASED METRICS, NOISY SCENARIO, PORTAL SEQUENCE.

Contaminant Number	SNR = 80 dB
1	57,15%
2	33,33%
3	25,53%

inside the bottle: at around half bottle height, at the interface between water and air, and on the bottom of the bottle (see black spheres in Fig. 10, in the first case it is hidden by reconstruction values). Moreover, an AWGN whose SNR= 80 dB is added to the computed scattering matrices.

The normalized reconstructed dielectric contrast is shown in Fig. 10. The contaminant is well detected in all the three considered positions, as also conformed by the proximity-based metrics, reported in Table VII, even if, as expected, the resolution is slightly inferior with respect to the previous case. Indeed, in this case the resolution in the medium, equivalent to half-wavelength at the selected frequency, is $R_w = \frac{\lambda_{w|2.25GHz}}{2} = 7.6\,\text{mm}$. Even so, this results prove the feasibility of the imaging procedure for lossy media.

IV. Conclusion and Perspectives

This work has presented the design and the numerical validation of a multi-antenna system to identify contaminants inside packaged food products moving along the production conveyor belt. The possible contaminant has been reconstructed, in the considered volume, via an imaging procedure where the dielectric contrast has been obtained with the TSVD algorithm enhanced with a novel illumination balancing algorithm. The system assessment has been performed in a realistic scenario considering industrial conveyor belt speeds, VNA acquisition times and adding noise to the synthetic data.

The outcomes of the study showed that the proposed MWI system is able to detect 2 mm PET plastic contaminants in both cases of hazelnut-cocoa cream jars and water bottles. In all cases, the contaminant has been well detected in its expected position within the considered product. As the detection of this kind of materials is almost impossible with commercial X-ray systems such a result motivates further activities aimed at realizing the designed system and performing its experimental validation in an industrial scenario. In doings so, the requirement in terms of spacing of the targets, which is anyhow acceptable in the industrial context, could be removed or relaxed by improving the propagation model exploited in the imaging algorithm. In addition, a proper shielding of the volume of interest would be necessary to avoid any kind of interference of the imaging system: a metal box, to protect the device from external noise, and a layer of absorbers on the inner surfaces to prevent multiple reflections.

Acknowledgment

This work was supported by the Italian Ministry of University and Research under the PRIN project "BEST-Food, Broadband Electromagnetic Sensing Technologies for Food Quality and Security Assessment."

References

[1] M. Edwards, *Detecting foreign bodies in food*. Woodhead Publishing Ltd, 2004.
[2] The rapid alert system for food and feed. [Online]. Available: https://ec.europa.eu/food/sites/food/files/safety/docs/rasff_annual_report_2018.pdf
[3] R. Haff and N. Toyofuku, "X-ray detection of defects and contaminants in the food industry," *Sensing and Instrumentation for Food Quality and Safety*, vol. 2, Dec. 2008.
[4] Eagle Product Inspection, "How to detect previously undetectable contaminants - white paper," Tech. Rep., January 2015. [Online]. Available: https://www.foodonline.com/doc/capabilities-and-limitations-of-food-x-ray-inspection-equipment-0001
[5] N. Lorenzi. (2019, January) Inspection and detection equipment reach new levels of flexibility for peak food safety. [Online]. Available: https://www.foodsafetystrategies.com/articles/613-inspection-and-detection-equipment-reach-new-levels-of-flexibility-for-peak-food-safety
[6] C. Nerin, "Plastics and polymers for food packaging manufacturing," in *Reference Module in Food Science*. Elsevier, 2016. [Online]. Available: http://www.sciencedirect.com/science/article/pii/B9780081005965031954
[7] U. Hurzlmeier. Sesotec food safety and x-ray: Single energy vs. dual energy technology detection of plastics & other low dense foreign bodies within meat industry. [Online]. Available: https://www.sesotec.com/emea/en/resources/blog/detection-of-plastics-with-x-ray-systems-in-the-food-industry
[8] P. Pallav, G. G. Diamond, D. A. Hutchins, R. J. Green, and T. H. Gan, "A Near-Infrared (NIR) Technique for Imaging Food Materials," *J. of Food Science*, vol. 74, pp. 23–33, 2009.
[9] J.-H. Qu, D. Liu, J.-H. Cheng, D.-W. Sun, J. Ma, H. Pu, and X.-A. Zeng, "Applications of near-infrared spectroscopy in food safety evaluation and control: A review of recent research advances," *Critical Reviews in Food Science and Nutrition*, vol. 55, no. 13, pp. 1939–1954, 2015, pMID: 24689758. [Online]. Available: https://doi.org/10.1080/10408398.2013.871693
[10] F. Becker, C. Schwabig, J. Krause, S. Leuchs, C. Krebs, R. Gruna, A. Kuter, T. Langle, D. Nuessler, and J. Beyerer, "From visual spectrum to millimeter wave: A broad spectrum of solutions for food inspection," *IEEE Antennas and Propagation Magazine*, vol. 62, no. 5, pp. 55–63, 2020.
[11] W.-H. Lee and W. Lee, "Food inspection system using terahertz imaging," *Microwave and Optical Technology Letters*, vol. 56, no. 5, pp. 1211–1214, 2014.
[12] [Online]. Available: http://terasense.com/applications/terahertz-food-inspection/

[13] Z. Wu and H. Wang, "Microwave tomography for industrial process imaging: Example applications and experimental results," *IEEE Antennas and Propagation Magazine*, vol. 59, no. 5, pp. 61–71, 2017.

[14] J. LoVetri, M. Asefi, C. Gilmore, and I. Jeffrey, "Innovations in electromagnetic imaging technology: The stored-grain-monitoring case," *IEEE Antennas and Propagation Magazine*, vol. 62, no. 5, pp. 33–42, 2020.

[15] J. A. Tobon Vasquez, R. Scapaticci, G. Turvani, M. Ricci, L. Farina, A. Litman, M. R. Casu, L. Crocco, and F. Vipiana, "Noninvasive inline food inspection via microwave imaging technology: An application example in the food industry," *IEEE Antennas and Propagation Magazine*, vol. 62, no. 5, pp. 18–32, 2020.

[16] F. Zidane, J. Lanteri, J. Marot, L. Brochier, N. Joachimowicz, H. Roussel, and C. Migliaccio, "Nondestructive control of fruit quality via millimeter waves and classification techniques: Investigations in the automated health monitoring of fruits," *IEEE Antennas and Propagation Magazine*, vol. 62, no. 5, pp. 43–54, 2020.

[17] M. Ricci, L. Crocco, and F. Vipiana, "Microwave imaging device for in-line food inspection," in *2020 14th European Conference on Antennas and Propagation (EuCAP)*, 2020, pp. 1–4.

[18] M. Ricci, L. Crocco, and F. Vipiana, "Microwave imaging system for in-line security assessment," in *Proc. IEEE International Symposium on Antennas and Propagation*, July 2020.

[19] Keysight Technologies, "M980xA Series PXIe Vector Network Analyzer," *Data Sheet*, 2020.

[20] D. O. Rodriguez-Duarte, J. A. Tobon Vasquez, R. Scapaticci, L. Crocco, and F. Vipiana, "Brick shaped antenna module for microwave brain imaging systems," *IEEE Antennas and Wireless Propagation Letters*, pp. 1–5, 2020.

[21] O. M. Bucci, L. Crocco, and R. Scapaticci, "On the optimal measurement configuration for magnetic nanoparticles-enhanced breast cancer microwave imaging," *IEEE Transactions on Biomedical Engineering*, vol. 62, no. 2, pp. 407–414, 2015.

[22] O. M. Bucci, L. Crocco, R. Scapaticci, and G. Bellizzi, "On the design of phased arrays for medical applications," *Proc. IEEE*, vol. 104, no. 3, pp. 633–648, Mar. 2016.

[23] R. Scapaticci, J. A. Tobon Vasquez, G. Bellizzi, F. Vipiana, and L. Crocco, "Design and numerical characterization of a low-complexity microwave device for brain stroke monitoring," *IEEE Trans. Antennas Propag.*, vol. 66, pp. 7328–7338, Dec. 2018.

[24] Jorge A. Tobon Vasquez et al., "Design and experimental assessment of a 2D microwave imaging system for brain stroke monitoring," *Int. J. Antennas Propag.*, no. Article ID 8065036, p. 12 pages, 2019.

[25] J. A. Tobon Vasquez, R. Scapaticci, G. Turvani, G. Bellizzi, D. O. Rodriguez-Duarte, N. Joachimowicz, B. Duchene, E. Tedeschi, M. R. Casu, L. Crocco, and F. Vipiana, "A prototype microwave system for 3D brain stroke imaging," *SENSORS*, vol. 20, May 2020.

[26] O. M. Bucci, C. Gennarelli, and C. Savarese, "Representation of electromagnetic fields over arbitrary surfaces by a finite and nonredundant number of samples," *IEEE Trans. Antennas Propagat.*, vol. 46, pp. 351–359, 1998.

[27] O. M. Bucci and G. Franceschetti, "On the degrees of freedom of scattered fields," *IEEE Transactions on Antennas and Propagation*, vol. 37, no. 7, pp. 918–926, 1989.

[28] O. M. Bucci and T. Isernia, "Electromagnetic inverse scattering: Retrievable information and measurement strategies," *Radio Science*, vol. 32, no. 6, pp. 2123–2137, 1997.

[29] M. Pastorino, "Microwave imaging," *Microwave Imaging*, 04 2010.

[30] D. Tajik, F. Foroutan, D. S. Shumakov, A. D. Pitcher, and N. K. Nikolova, "Real-time microwave imaging of a compressed breast phantom with planar scanning," *IEEE J. of Electromagnetics, RF, and Microwaves in Medicine and Biology*, vol. 2, no. 3, pp. 154–162, 2018.

[31] A. S. Beaverstone, D. S. Shumakov, and N. K. Nikolova, "Frequency-domain integral equations of scattering for complex scalar responses," *IEEE Trans. on Microwave Theory and Tecniques*, vol. 65, no. 4, pp. 1120–1132, 2017.

[32] E. A. Attardo, A. Borsic, G. Vecchi, and P. M. Meaney, "Whole-system electromagnetic modeling for microwave tomography," *IEEE Antennas Wirel. Propag. Lett.*, vol. 11, pp. 1618–1621, 2012.

[33] D. O. Rodriguez-Duarte, J. A. Tobon Vasquez, R. Scapaticci, L. Crocco, and F. Vipiana, "Assessing a microwave imaging system for brain stroke monitoring via high fidelity numerical modelling," *IEEE Journal of Electromagnetics, RF and Microwaves in Medicine and Biology*, 2021.

[34] M. Bertero and P. Boccacci, *Introduction to Inverse Problems in Imaging*. Inst. Phys., Bristol, U.K., 1998.

[35] R. Scapaticci, V. Lopresto, R. Pinto, M. Cavagnaro, and L. Crocco, "Monitoring thermal ablation via microwave tomography: An ex vivo experimental assessment," *Diagnostics*, vol. 8, no. 4, 2018. [Online]. Available: https://www.mdpi.com/2075-4418/8/4/81

[36] SCS Service and Calibration Solutions. [Online]. Available: https://scsukltd.com/product/x-ray-test-pieces/